SUPPLEMENTARY MATERIAL

Strain-engineered inverse charge-funnelling in layered semiconductors

Adolfo De Sanctis, Iddo Amit, Steven P. Hepplestone, Monica F. Craciun, and Saverio Russo*

Centre for Graphene Science, College of Engineering, Mathematics and Physical Sciences, University of Exeter, Exeter EX4 4QF, United Kingdom

E-mail: S.Russo@exeter.ac.uk

Contents

S1 Photo-oxidation mechanism **3**

S2 Supplementary AFM and spectroscopy data **5**

S2.1 Laser-induced oxidation: AFM data 5

S2.2 Photon assisted oxidation of bulk HfS_2 7

S2.3 Supplementary AFM data 8

S2.4 Visible wavelength absorption and photoluminescence extended data 9

S3 First principles calculations **10**

S3.1 Reactions energy cost 10

S3.2 HfS_2 and HfO_2 band structure 11

*To whom correspondence should be addressed

S4 Supplementary photoresponse data 12

S4.1 Electrical characterization 12

S4.2 Extended photocurrent mapping data 12

S5 Analytical model describing the observed SPCM response 14

S6 Supplementary discussion on PV enhancement using charge funnelling 18

S1 Photo-oxidation mechanism

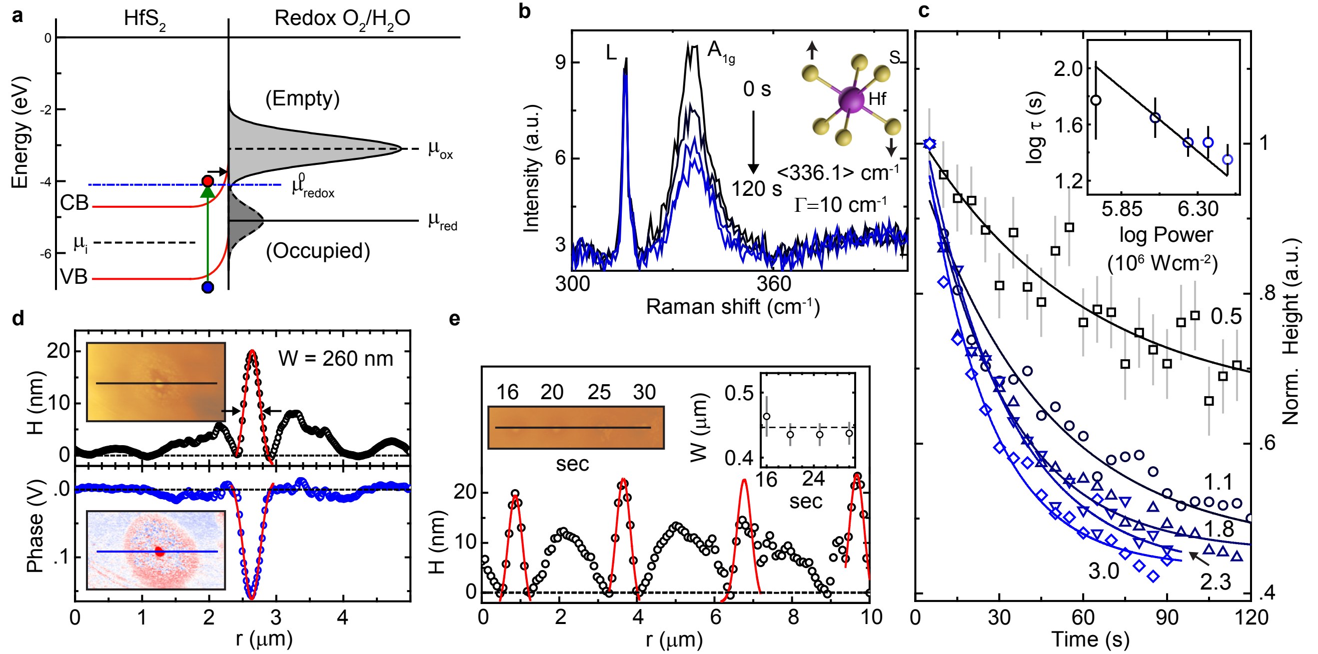

Figure S1: **Charge-Transfer model and photo-oxidation of HfS_2.** **a**, Schematic energy diagram of multi-layer HfS_2 in contact with the redox couple O_2/H_2O present in air in atmospheric conditions.[1] The chemical potentials of the oxidizing and reducing species are $\mu_{ox} = -3.1$ eV and $\mu_{ox} = -5.1$ eV, respectively. The chemical potential of the oxygen acceptor state is $\mu^0_{redox} = -4.1$ eV. The intrinsic work function of HfS_2 is $\mu_i = -5.7$ eV with $E_g = 1.96$ eV. **b**, Time evolution of the HfS_2 A_{1g} Raman mode at $336.1 \pm 0.01\,\mathrm{cm}^{-1}$ (average), with FWHM $10\,\mathrm{cm}^{-1}$, upon laser exposure ($\lambda = 514$ nm, P = 3.0 MW/cm^2) of a 4.9 nm thick flake. The peak named L corresponds to a spurious laser line (note no change of this line in the spectra). **c**, Normalized A_{1g} mode height as a function of time for different incident laser powers (0.5 - 3.0 MW/cm^2), solid lines mark monoexponential decays; Inset: log-log plot of decay time τ versus incident power density, solid line marks a slope of -1. **d**, AFM topography (top) and phase signal (bottom) of a 80 nm-thick laser-irradiated flake ($\lambda = 375$ nm, P = 1.5 MW/cm^2, 10 seconds exposure), a Gaussian peak can be fitted with a FWHM of 260 nm. **e**, AFM topography of the same flake with laser-irradiated spots for different exposure times ($\lambda = 473$ nm, P = 4.3 MW/cm^2). Inset: FWHM of the Gaussian fits as a function of exposure time, dashed line marks the average value of 446 nm.

Following the model in ref. 2, we propose in figure S1a the energy diagram of the interface between HfS_2 and aqueous oxygen in atmosphere[1] provided by the reaction $2H_2O \rightleftharpoons O_2(aq) + 4e^- + 4H^+$. The intrinsic chemical potential of HfS_2 is $\mu_i = -5.2$ eV (calculated from the distance from the vacuum level to the top of the valence band, $\phi = -6.68$ eV and

indirect bandgap $E_g = 1.96$ eV), while that of the oxygen acceptor state is $\mu^0_{redox} = -4.1$ eV. This induces a band-bending at the surface of the layered semiconductor such that an optical transition above the bandgap can make an electron ready to be transferred to the oxygen empty states, making the photo-oxidation reaction highly feasible across the whole visible range, explaining the high instability of few-layer HfS_2 in atmospheric conditions. The CT reaction starts with a photon of energy hν impinging on HfS_2, which produces an optical excitation, leaving the material in an excited state: $HfS_2 + h\nu \longrightarrow {HfS_2}^*$. This state provides the carriers for the CT reaction at the surface according to the following:

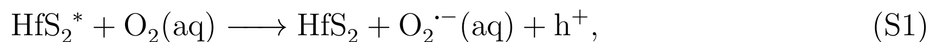

$$ {HfS_2}^* + O_2(aq) \longrightarrow HfS_2 + {O_2}^{\cdot -}(aq) + h^+, \tag{S1} $$

the oxygen radical ion ${O_2}^{\cdot -}(aq)$ can then react with the HfS_2 and, upon cleavage of the Hf−S bond, bind to the Hf and S, respectively:

$$ Hf + 2S + 3{O_2}^{\cdot -}(aq) + 3h^+ \longrightarrow HfO_2 + 2\,SO_2(g). \tag{S2} $$

Therefore the total reaction can be written as:

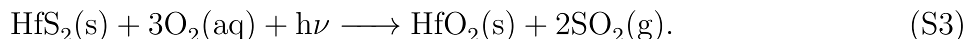

$$ HfS_2(s) + 3O_2(aq) + h\nu \longrightarrow HfO_2(s) + 2SO_2(g). \tag{S3} $$

Marcus-Gerischer theory (MGT)[1] gives an estimation of the rate of change in the pristine material composition:

$$ \frac{d\Theta}{dt} \propto \Theta \Phi_{ph}[O_2] \exp\left[-\frac{\left(\frac{E_g}{2} + E_i - E^0_{F,red} - \lambda\right)^2}{4k_b T\lambda} \right], \tag{S4} $$

where Θ is the amount of pristine material, Φ_{ph} is the laser flux, $[O_2]$ is the oxygen concentration, E_g is the direct gap energy, E_i is the intrinsic Fermi level, $E^0_{F,red}$ is the energy of the oxygen acceptor state (~ 3.1 eV) with respect to the vacuum level, λ is the renormalization energy of oxygen in water (~ 1 eV), k_b is the Boltzmann constant and T the temperature.[1]

Therefore, the oxidation rate depends on the laser flux Φ_{ph} and the initial amount of pristine material Θ_0: $\Theta \propto \Theta_0 \exp(-t/\tau)$ where the decay time $\tau \propto \Phi_{ph}^{-1}$. This dependence is experimentally verified in figure S1b-c where the intensity of the Raman A_{1g} mode of HfS_2, an indication of the amount of pristine material present in the sampling volume, is plotted against time for different laser fluxes. Monoexponential decay fits give a decay time τ with the expected power relation (figure S1c, inset).

Figure figure S1d shows that the oxidized area is compatible with the diffraction-limited spot size of our laser system (see methods). Indeed, the AFM topography and tapping phase images of an exposed thick (80 nm) flake shows a bubble-like structure with a 25 % increase in height. This feature shows a Gaussian profile with a full-width at half-maximum (FWHM) of 260 nm. We then exposed different areas of the flake, for different lengths of time while keeping the laser power density constant. As shown in figure S1e, no changes in the FWHM of the Gaussian profile is observed. All these observations confirm that photon-assisted oxidation is taking place, as opposed to thermal oxidation.

S2 Supplementary AFM and spectroscopy data

S2.1 Laser-induced oxidation: AFM data

In figure S2 we report additional data on the laser-induced oxidation process in HfS_2. Figure S2a-d show the AFM data acquired on a flake with different layers deposited on a Si/SiO_2 substrate (oxide thickness 285 nm). Different areas of the flake were exposed with $\lambda_{\text{exc}} = 532$ nm at a power of 0.1 MW/cm^2 for 20 s, using a commercial *Renishaw* micro-Raman spectroscopy system. A marked change of contrast in the areas of HfS_2 exposed to the laser is visible in the white light optical micrograph (see figure S2a). Though the observed change of contrast might suggest that HfS_2 has been ablated by the laser, a detailed study of the topography of the flakes with atomic force microscopy demonstrates that this is not the case, see figure S2b. Indeed, we measured that the average height of the laser-exposed area is the

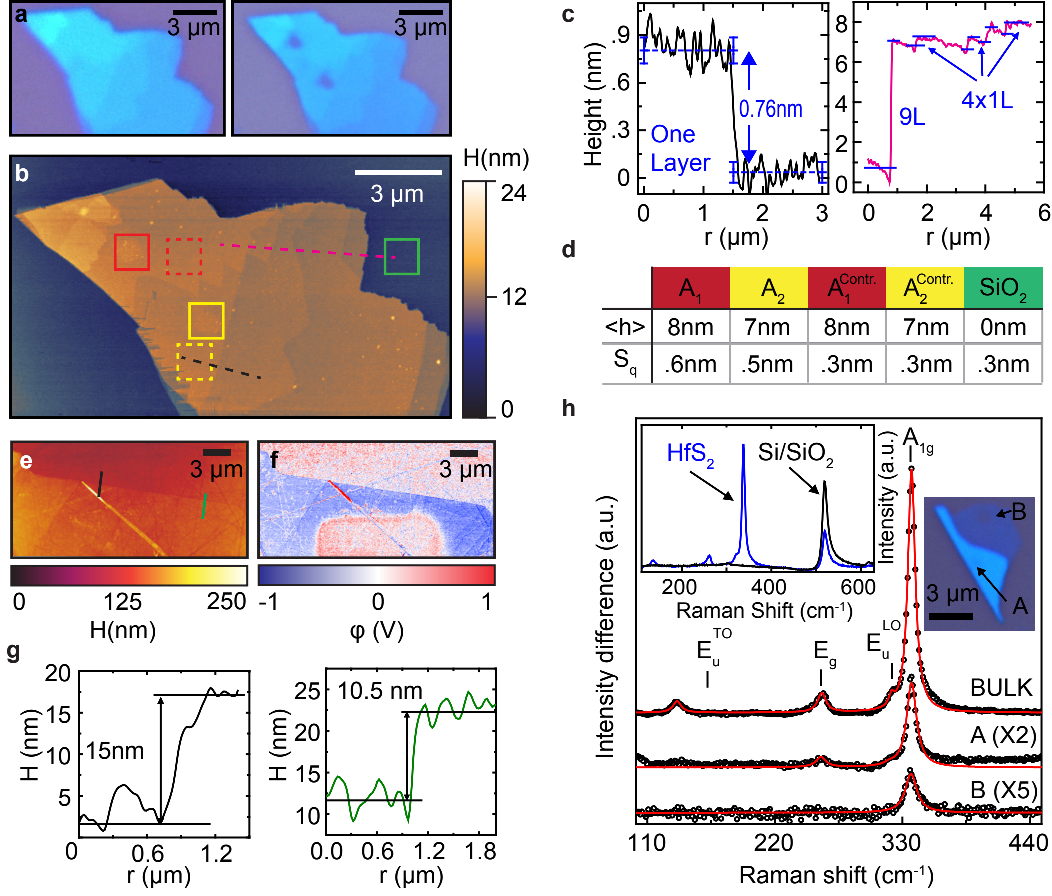

Figure S2: **Supplementary AFM data on laser-induced oxidation.** **a**, Optical micrographs of an HfS_2 flake before (left) and after (rigth) exposure of two areas with $\lambda_{exc} = 532$ nm at 0.1 MW/cm^2 incident power for 20 s. **b**, AFM topography of the same flake shown in **a**. The straight dashed lines correspond to the regions for profiles shown in panel **c**, where the height of a single layer is measured to be 0.76 ± 0.08 nm. Solid squares enclose the laser-exposed regions, dashed squares enclose the control regions used for statistical analysis. **d**, Statistical analysis of AFM topography shown in **b**: $< h >$ is the average height measured in the square and S_q is the RMS surface roughness. **e**, AFM topography and **f** tapping phase images of the HfS_2 flake presented in Figure 1a main text, after laser exposure of the central area. **g**, Height profiles across the solid lines shown in **e**. **h**, Raman spectra of HfS_2 acquired on a bulk sample (> 100 μm thick) and on a thinner flake exfoliated on Si/SiO_2 (areas A and B in the optical micrograph), after subtraction of the pristine substrate spectrum (inset).

same as the nearby control area (figure S2d), $< \mathrm{h} > \simeq 8$ nm, while the RMS height of the surface (roughness), $\mathrm{S_q}$, is increased by $\sim 50\%$ with respect to the control areas (which have an $\mathrm{S_q}$ value comparable with that of the underlying substrate).

Figure S2e-g show additional AFM data for the flake of figure 1 in the main text. The AFM topography and tapping phase images are shown in panels e and f, respectively. Panel g shows the height profiles for the two different regions of the flake. The height of one layer of $\mathrm{HfS_2}$ was measured to be 0.76 ± 0.08 nm (panel c), thus the aforementioned flake has a thickness of ~ 20 and ~ 14 layers in the two regions across which the laser was scanned.

In figure S2h we report the Raman spectra of $\mathrm{HfS_2}$ on a $\mathrm{Si/SiO_2}$ substrate, shown in the optical micrograph inset. In the bulk material we observe all the first order Raman modes: $\mathrm{A_{1g}} = 337\ \mathrm{cm^{-1}}$, $\mathrm{E_g} = 260\ \mathrm{cm^{-1}}$, $\mathrm{E_u(LO)} = 321\ \mathrm{cm^{-1}}$ and $\mathrm{E_u(TO)} = 136\ \mathrm{cm^{-1}}$; All these modes are well described by a fit with a Lorentzian curve with a FWHM $\sim 10\ \mathrm{cm^{-1}}$ and the peak positions agree well with previous studies,[3–5] except for the $\mathrm{E_u(TO)}$ mode which appears blue-shifted (literature value $\sim 155 - 166\ \mathrm{cm^{-1}}$). For thinner flakes we observe that it is increasingly difficult to acquire a spectrum as the material is thinned. To the best of our knowledge no reports have shown the isolation of single-layer $\mathrm{HfS_2}$.

S2.2 Photon assisted oxidation of bulk $\mathrm{HfS_2}$

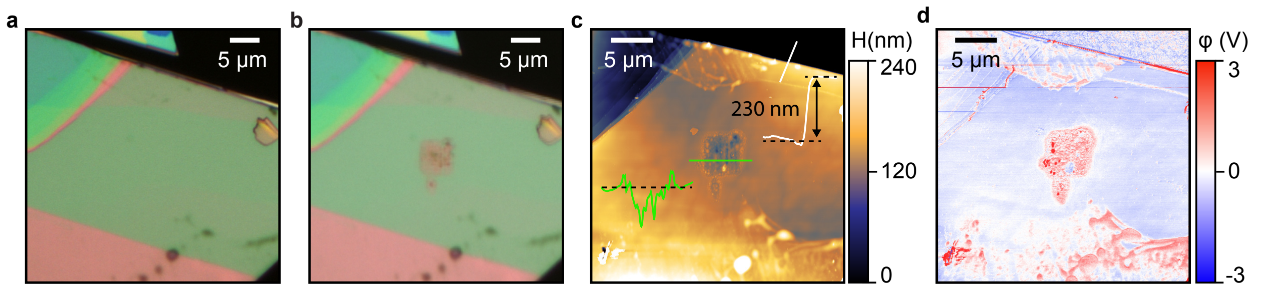

Figure S3: **Thick flakes photo-oxidation and damage. a-b**, Optical micrograph of a thick flake before (**a**) and after (**b**) laser exposure of a 5×5 μm square, with $\lambda_{\mathrm{exc}} = 375$ nm ($P = 5.0$ MW/cm^2), scanned in steps of 0.5 μm, exposing each point for 20 s. **c-d**, AFM topography (**c**) and tapping phase (**d**) images of the flake shown in **a**. Insets show the thickness of the flake (white), $\delta = 230$ nm, and the height profile of the laser exposed area (green), the black dotted line marks the average height of the pristine flake.

65 Figure S3 shows the photo-oxidation of a thick (230 nm) HfS_2 flake. A comparison of
66 micrograph pictures before (figure S3a) and after (figure S3b) exposing with a laser a 5×5
67 μm square area ($\lambda_{exc} = 375$ nm, $P = 5.0$ MW/cm^2, 0.5 μm steps each exposed for 20 s)
68 shows that for bulk flakes the oxidation does not involve the whole thickness, as it is not
69 possible to see the substrate underneath the flake. Indeed, AFM topography (figure S3c)
70 and tapping phase (figure S3d) show that the surface of the flake is damaged after prolonged
71 exposure, as shown by the line profiles across the laser-exposed region.

72 S2.3 Supplementary AFM data

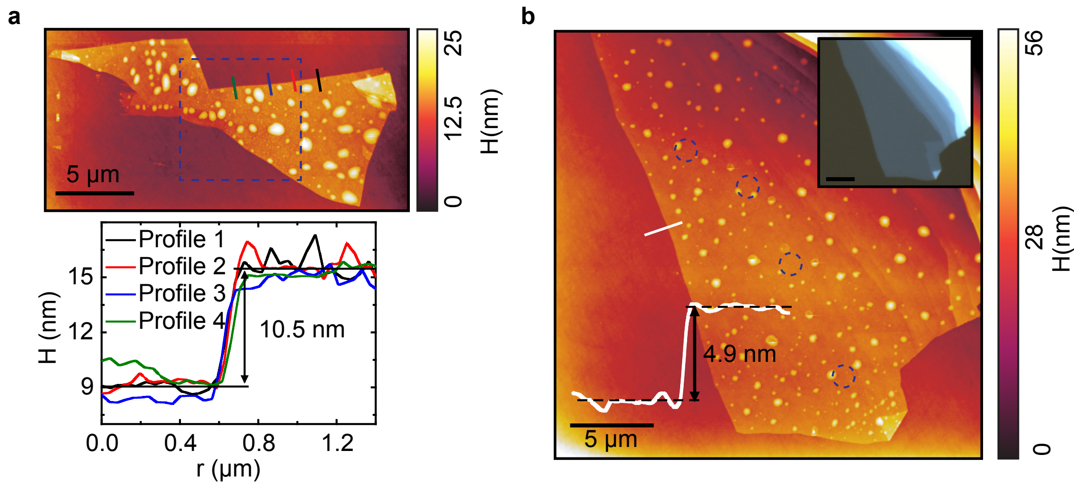

Figure S4: **Absorption coefficient and photooxidation AFM data. a**, AFM topography (top) of the HfS_2 flake presented in figure 3a, main text, after laser exposure of the area marked by the dotted square (see main text). Height profiles across the solid lines are shown in the bottom panel: an average flake thickness of 10.5 nm is reported, corresponding to $\sim$ 14 layers. **b**, AFM topography of the flake used in the photooxidation study shown in figure 2, main text. Dashed circles mark the position where the Raman signal was acquired as a function of time. The flake thickness is 4.9 nm, corresponding to $\sim$ 7 layers. Inset: optical micrograph of the flake immediately after exfoliation on Quartz substrate.

73 The data regarding the absorption coefficient, presented in figure 4 in the main text and
74 in figure S5, have been acquired on a 10.5 nm thick flake, as shown in Figure S4a. The data
75 shown in figure 2c in the main text have been acquired on a uniform 4.9 nm thick flake, as
76 shown in figure S4b.

S2.4 Visible wavelength absorption and photoluminescence extended data

Figure S5a shows the absorption coefficient of pristine HfS_2 as acquired on a thin flake in our experimental setup (see methods). The data are in good agreement with the literature.[6] Transmittance (T), reflectance and absorbance (1-T-R) are shown in figure S5b. Figure S5c shows the photoluminescence (PL) spectra of two representative flakes of bulk HfS_2 under 473 nm excitation. No strong exciton peak can be seen in proximity of the indirect gap energy whilst the feature at ~ 1.7 eV has been attributed to impurity states in the gap.[7]

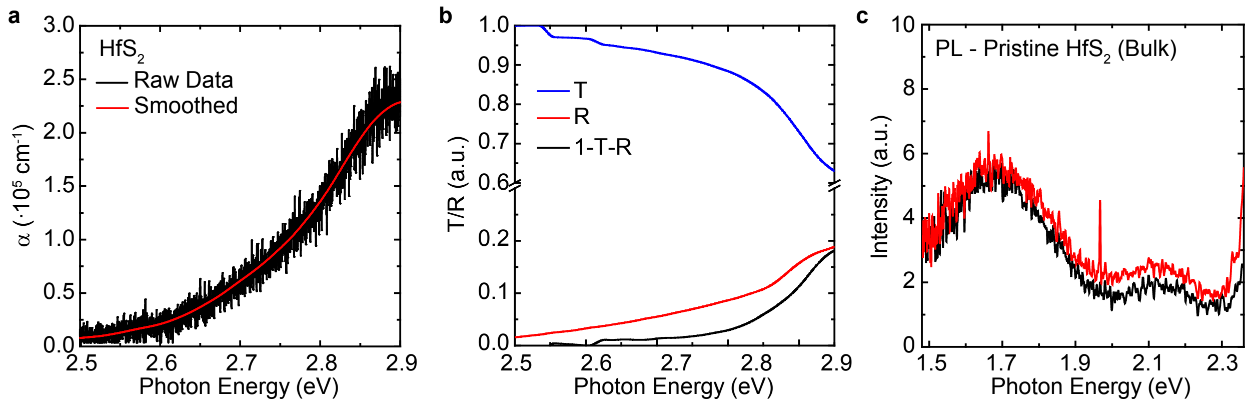

Figure S5: **Absorption coefficient α of pristine HfS_2.** **a**, α as a function of photon energy in the visible range, as shown in figure 4a, main text. Raw (black) and smoothed (red) data are presented. **b**, Normalised transmittance (T), reflectance (R) and absorbance (1-T-R) as a function of photon energy. **c**, Photoluminescence (PL) spectra of two representative flakes of bulk HfS_2 under 473 nm excitation.

85 # S3 First principles calculations

86 ## S3.1 Reactions energy cost

87 The feasibility of the reaction in equation (S3) has been verified by simulating the crystal
88 structure of the different compounds and calculating the energy cost per reaction, as shown
in figure S6 and table S1. The energy cost was calculated as $E_{\mathrm{R}} = E_{\mathrm{reagents}} - E_{\mathrm{products}}$.

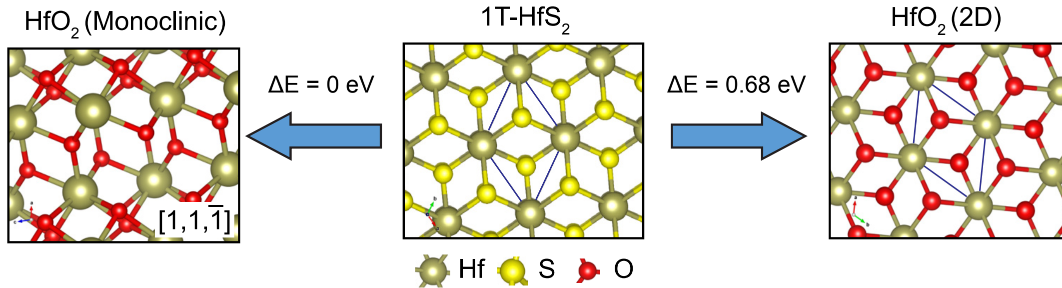

Figure S6: **Reactions energy cost and crystal structures** Simulated crystal structures and energy costs of the proposed reactions. The energy difference ΔE is calculated with respect to the formation of monoclinic HfO_2 (E = −11.58 eV). Unit cell highlighted in blue.

89

Table S1: Reactions energetics

Reaction	Energy cost (eV)	Energy cost (eV) per HfS_2	ΔE (eV)[a] per HfS_2
$HfS_2 + 3\,O_2 \longrightarrow HfO_2 + 2\,SO_2$[b]	-11.58	-11.58	
$32\,HfS_2 + (32 + 64\,)O_2 \longrightarrow Hf_{32}O_{64} + 64\,SO_2$[c]	-370.55	-11.58	
$HfS_2 + 3\,O_2 \longrightarrow HfO_2(2\,D) + 2\,SO_2$[f]	-10.90	-10.90	0.68
$HfS_2 + 3\,O_2 \longrightarrow HfO_2(\text{cubic}) + 2\,SO_2$[g]	-11.28	-11.28	0.30

[a]Compared to lowest energy reaction; [b]$1 \times 1 \times 1$ Primary unit cell of monoclinic HfO_2; [c]Large $2 \times 2 \times 2$ unit cell of monoclinic HfO_2; [f]Energy cost to produce 2D HfO_2; [g]Energy cost to produce cubic HfO_2;

90 We also considered the possibility of the formation of two-dimensional (2D) HfO_2, as
91 opposed to monoclinic 3D HfO_2. Such material would be given by the substitution of each
92 S by O in the 2D precursor. However, our calculation shows that the proposed reaction in
93 equation (S3) has an energy cost of −10.90 eV for 2D HfO_2, a difference ΔE = 0.68 eV as
94 compared to 3D (monoclinic) HfO_2, which makes the formation of 2D HfO_2 not favourable.

S3.2 HfS_2 and HfO_2 band structure

In figure S7a,b we report the calculated band structures of monoclinic HfO_2 and HfS_2, respectively. In the latter the indirect band gap is $\sim$ 1.38 eV in the $\Gamma \rightarrow$ M direction, while the direct gap at the Γ point is $\sim$ 2.1 eV. These values are $\sim$ 40% off the measured ones[6,8] and in line with other reported DFT calculations.[9] Figure S7c shows the calculated conduction band minimum (CBm) and valence band maximum (VBM) at Γ and in the $\Gamma \rightarrow$ M direction, as a function of strain. Figure S7d shows the energy difference between the strained and unstrained VBM and CBm.

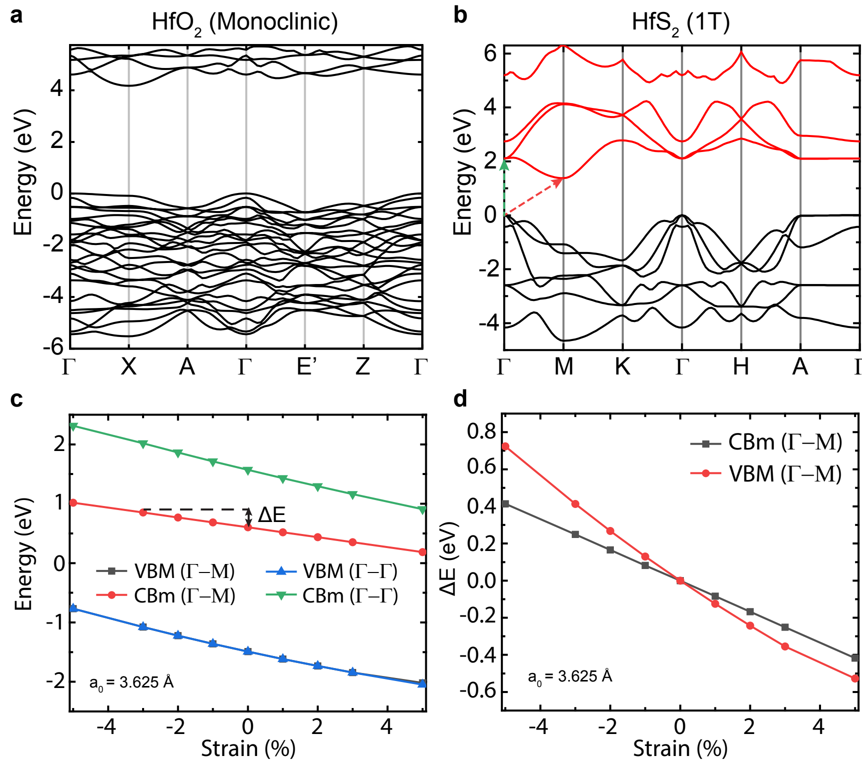

Figure S7: **Band structures of examined compounds.** **a**, Calculated band structure of monoclinic HfO_2. **b**, Calculated band structure of 1T-HfS_2. The energy scale is relative to the highest occupied state (0 eV). Black (red) are valence (conduction) states. **c**, Conduction band minimum (CBm) and valence band maximum (VBM) in the $\Gamma - \Gamma$ direction (red arrow in panel **b**) and in the $\Gamma -$ M direction (green arrow in panel **b**), as a function of strain. **d**, Difference between the unstrained and strained VBM and CBm in the $\Gamma -$ M direction.

S4 Supplementary photoresponse data

S4.1 Electrical characterization

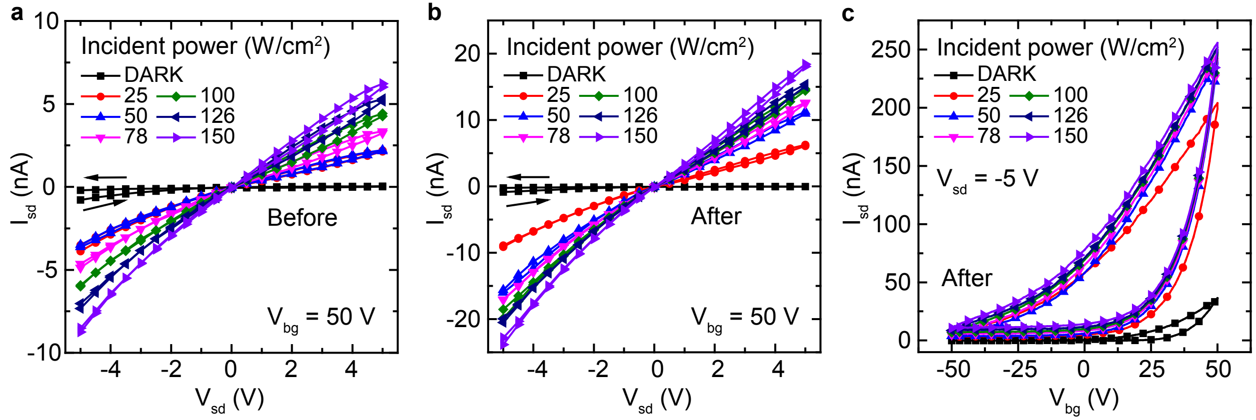

Figure S8: **Electrical characteristic of HfS_2 devices.** **a**, Current-voltage (I_{sd}-V_{sd}) characteristic of the device shown in figure 3 main text, before laser-assisted oxidation in the dark and for different incident optical powers ($\lambda = 473$ nm, $V_{bg} = +50$ V). **b**, Current-voltage characteristic of the same device after laser-assisted oxidation. **c**, Gate voltage dependence of the photocurrent for the same device, after laser-assisted oxidation, $V_{sd} = -5$ V.

Figure S8 shows the electrical characterization of the device presented in figure 3 in the main text. Figure S8a shows the current-voltage (I_{sd}-V_{sd}) characteristic before the photo-oxidation at different incident optical powers and figure S8b shows the same after the photo-oxidation. Sweeping the V_{sd} in both direction, no significant hysteresis is observed. In figure S8c we show a gate voltage sweep as a function of incident optical power for the same device. In this case a very large hysteresis is observed, due to the ambient contamination of the device since it is measured in air at room temperature. The observed hysteresis is in agreement with previous results.[10]

S4.2 Extended photocurrent mapping data

Figure S9a shows the scanning photocurrent microscopy (SPCM) map of the device presented in Figure 4 of the main text, prior to laser-assisted oxidation. Under a bias of $V_{sd} = \pm 1$ V, the map shows a very small photocurrent generated in the flake, which does not change

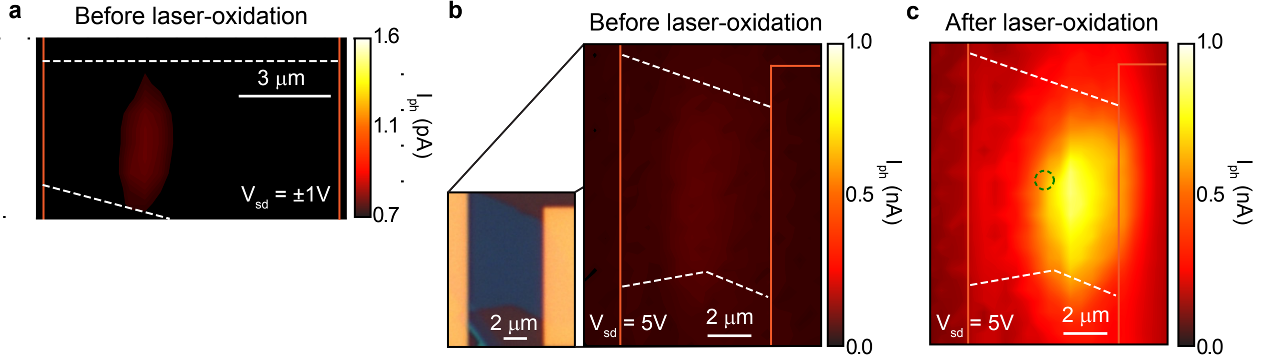

Figure S9: **Extended photocurrent data of HfS_2 devices.** **a**, Scanning photocurrent microscopy map (SPCM) of the device in Figure 4, main text, before laser assisted oxidation. Under $V_{sd} = \pm 1\,\text{V}$ only a small photocurrent is observed. For $V_{sd} = 0\,\text{V}$ no photoresponse could be measured at the sensitivity of our instruments. **b-c**, SPCM maps of another device before and after (**c**) laser assisted oxidation in the centre of the flake (green circle), under $V_{sd} = 5\,\text{V}$. Optical micrograph of the device is shown in panel **b**, inset. All SPCM measurements were performed using $\lambda = 473$ nm at a power $P = 150$ W/cm^2, as in Figure 4, main text.

117 with the sign of the bias. Therefore we attribute this small contribution to impurities on
118 the surface causing local doping of the material. No measurable photocurrent was recorded
119 at zero bias. Figure S9b-c show the SPCM maps of another device before and after laser
120 assisted oxidation in the centre of the flake, under $V_{sd} = 5\,\text{V}$. This device shows the same
121 behaviour as the one presented in Figure 3, main text, where a strong localized photocurrent
122 is observed after laser-assisted oxidation (green circle). Before laser oxidation no significant
123 photocurrent can be observed, as in the previous case.

124
S5 Analytical model describing the observed SPCM response

126 In this section we develop a simple analytical model which allows to simulate the scanning
127 photocurrent microscopy (SPCM) results shown in the main text (see figure 4f).

128 In order to describe how local illumination results in a spatial map of the photoresponse
129 of a device we need to consider the processes of generation, motion and collection of charges.
130 Starting from the charge continuity equation:

$$\frac{1}{q}\frac{\partial \rho}{\partial t} = G - R - \frac{1}{q}\boldsymbol{\nabla}\cdot\mathbf{j}, \tag{S5}$$

131 where ρ is the charge density, G and R are the generation and recombination rates of the
132 carriers, respectively and $\mathbf{j}$ is the current density. Assuming that the average carriers diffusion
133 length is larger than the laser-spot size we can take G to be a delta function centred at the
134 laser excitation point. The recombination rate is equal to $R_i = -{}^{\Delta n_i}/_{\tau_i}$, where $i = e, h$
135 indicates the two types of carrier, τ is the carrier recombination lifetime and $\Delta n_i = n_i^t - n_i^d$
136 is the excited carriers density (difference between the total carrier density n_i^t and the carrier
137 density in absence of illumination n_i^d). The carrier density can be decomposed into drift and
138 diffusion terms (we neglect thermoelectric effects):

$$\mathbf{j} = q(n_e\mu_e - n_h\mu_h)\mathbf{E} + q(D_e\boldsymbol{\nabla}n_e - D_h\boldsymbol{\nabla}n_h), \tag{S6}$$

139 where μ_i is the mobility, $\mathbf{E}$ is the electric field across the device and $D_i = (k_bT\mu_i)/q$ is the
140 diffusion coefficient at temperature T with $k_b \simeq 8.617\cdot 10^{-5}\,\mathrm{eV/K}$ the Boltzmann constant.
141 In a junction device or in the presence of a Schottky contact the photocurrent is dominated
142 by the minority carriers since the drift and diffusion components of the majority carriers will
143 cancel each other.[11] It is therefore possible to recast equation (S5) in terms of one type of
144 carrier:

$$\frac{\partial n_e}{\partial t} = -\frac{\Delta n_e}{\tau_e} - \frac{1}{q}\boldsymbol{\nabla}\cdot\mathbf{j_e}. \tag{S7}$$

145 It is important to notice the spatial dependence of Δn_e and $\mathbf{E}$. Therefore, for a 1D system,
146 equation (S7) takes the form:

$$\frac{\partial n_e}{\partial t} = -\frac{\Delta n_e}{\tau_e} - \mu_e \Delta n_e \frac{\partial E}{\partial x} + \mu_e E \frac{\partial \Delta n_e}{\partial x} + D_e \frac{\partial^2 \Delta n_e}{\partial x^2}. \tag{S8}$$

147 Solving equation (S8) for the steady-state ${}^{\partial n_e}/_{\partial t} = 0$, we obtain:

$$\frac{\partial^2 \Delta n_e}{\partial x^2} + \frac{\mu_e}{D_e} E(x) \frac{\partial \Delta n_e}{\partial x} - \left(\frac{1}{\tau_e D_e} + \frac{\mu_e}{D_e}\frac{\partial E(x)}{\partial x}\right)\Delta n_h = 0. \tag{S9}$$

148 The solution of equation (S9) allows to know Δn_e in each point away from the illumination
149 and, therefore, the current can be calculated as:

$$I = -q \int_0^L \left(n_e(x)\mu_e E(x) + D_e \frac{\partial \Delta n_e(x)}{\partial x}\right) dx, \tag{S10}$$

150 where the integral is carried out along the length of the device L.

151 In order to solve equation (S9) the electric field distribution $E(x)$ is required. Depending
152 on the band structure and the energy profile of photoexcited particles, three type of funnelling
153 mechanisms are possible:[12] (1) Type I funnel, where the energy level of electrons continuously
154 decreases towards the region of strain, while that of holes increases; (2) Type II funnel, where
155 both levels decrease with increasing strain and the exciton binding energy is small (weakly
156 bound excitons); (3) Type III funnel, in which the behaviour of the bandgap is the same as
157 in type II but in the presence of strongly bound excitons. From the bandgap profiles shown
158 in Figure 1b of the main text, and from the absence of a strong excitonic peak in the PL
159 spectrum of HfS2 (see figure S5), we conclude that our device is a Type II funnel. In this
160 case, due to the weak exciton binding energy, it is possible to replace the potential gradient
161 generated by the strain-induced bandgap modulation with and effective electric field. The

162 simplest model we can adopt is a linear potential from the strained interface (x_j) across a
163 region of length l_j, as depicted schematically in figure S10. The corresponding electric field
164 $E = -\boldsymbol{\nabla} V$ is given by:

$$E(x) = \begin{cases} -\frac{V_{sd}}{L} \pm \frac{V_0}{l_j}, & x_j - \frac{l_j}{2} \leq x \leq x_j + \frac{l_j}{2} \\ -\frac{V_{sd}}{L}, & \text{otherwise} \end{cases} = \begin{cases} -E_{sd} \pm E_0, & x_j - \frac{l_j}{2} \leq x \leq x_j + \frac{l_j}{2} \\ -E_{sd}, & \text{otherwise} \end{cases}, \tag{S11}$$

165 which represents the superposition of the applied electric field E_{sd} and the built-in field due
166 to the strain-induced bandgap modulation E_0. The plus (minus) sign applies to the left
167 (right) junction, respectively. It is important to notice that the sign of E_{sd} depends on the
168 applied bias, whilst the sign of E_0 depends on the bandgap gradient and it is fixed at each
169 strain junction. Using equation (S11) in equation (S10) we obtain:

$$\Delta n_e = \begin{cases} \Delta n_e^0 \exp\left\{ -\frac{1}{2} \left(\frac{q}{k_B T}(E_{sd} \pm E_0) + \sqrt{\left(\frac{q}{k_B T} \left(E_{sd} \pm E_0 \right) \right)^2 + \frac{4}{\tau_e D_e}} \right) |x - x_0| \right\}, & x_j - \frac{l_j}{2} \leq x \leq x_j + \frac{l_j}{2} \\ \Delta n_e^0 \exp\left\{ -\frac{1}{2} \left(\frac{q}{k_B T} E_{sd} + \sqrt{\left(\frac{q}{k_B T} \right)^2 E_{sd}^2 + \frac{4}{\tau_e D_e}} \right) |x - x_0| \right\}, & \text{otherwise} \end{cases}, \tag{S12}$$

170 where Δn_e^0 is the excited carrier density at the injection (illumination) point $x = x_0$. We
171 can therefore use equation (S12) and equation (S10) to simulate an SPCM experiment by
172 calculating the total charge injected in the channel at each injection point $0 \leq x_0 \leq L$,
173 taking into account that in the oxide region ($x_{ox} - \frac{l_{ox}}{2} \leq x \leq x_{ox} + \frac{l_{ox}}{2}$, see figure figure S10)
174 $\Delta n_e^0 = 0$, since the bandgap of the oxide is greater than the energy of the impinging photon.

175 The fit shown in figure 4f, main text, is performed using a value of mobility of $\mu_e =$
176 $2.4\,\mathrm{cm^2V^{-1}s^{-1}}$, which is typical for these devices.[13] The injected charges can be estimated
177 from the photon flux $\phi = P_{laser}/E_{laser} \simeq 3.5 \cdot 10^{20}\,\mathrm{s^{-1}cm^{-2}}$ and the internal quantum efficiency
178 $\eta_i = (I_{ph}E_{laser}/qP_{laser})/(1 - R - T) \simeq 3.0 \cdot 10^{-4}$ (where R and T are the reflectivity and
179 transmittance, respectively, as shown in figure S5b), which give a value of injected carriers

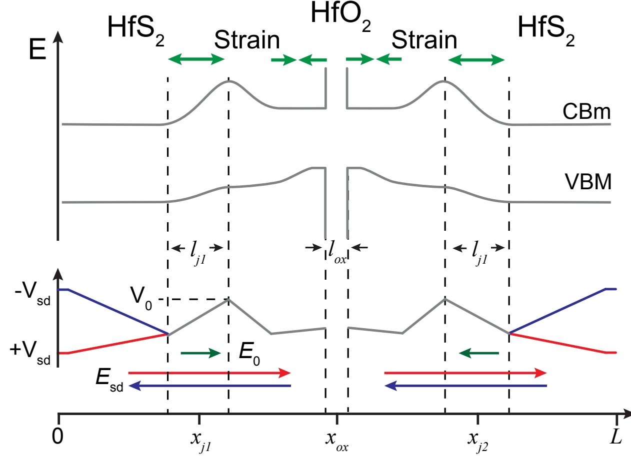

Figure S10: **SPCM model in a strained device.** Schematic band diagram of a strained device with the oxide region at the centre of the channel. There are four strain regions (green arrows), two compressive in the vicinity of the oxide and two tensile far away from it. The simplified potential is shown below for positive ($+V_{sd}$) and negative ($-V_{sd}$) bias.

180 $\Delta n_e^0 = 1.05 \cdot 10^{17}\,\text{s}^{-1}\text{cm}^{-2}$. The value of the built-in potential is taken as the difference
181 between the conduction band minimum (CBm) of the strained and unstrained semiconductor,
182 as shown in figure S7c-d, and it is equal to $V_0 = 0.24\,\text{V}$. The length of the channel is
183 $L = 26\,\mu\text{m}$ and $T = 300\,\text{K}$. The position of the strained junctions can be determined
184 from figure 2, main text: $l_{j1} = 2.5\,\mu\text{m}$ (left) and $l_{j2} = 2.0\,\mu\text{m}$ (right) while the oxide
185 region is $x_{ox} = 15.0\,\mu\text{m}$ and $l_{ox} = 1.0\,\mu\text{m}$. The carriers lifetime, dominated by non-radiative
186 recombination, is left as a free parameter since, to the best of our knowledge, no experiments
187 are reported in literature with measurement of this value for HfS_2. We find that to obtain a
188 good fit and reproduce qualitatively the experimental data we have to assume two different
189 relaxation times for the strained (τ_1) and unstrained (τ_2) regions. We find $\tau_1 \simeq 1 \cdot 10^{-6}\,\text{s}$
190 and $\tau_2 \simeq 1 \cdot 10^{-12}\,\text{s}$. The two different values could be explained by a change in electron-hole
191 binding energy due to strain, as previously suggested for different materials.[14]

192 # S6 Supplementary discussion on PV enhancement us-
193 ing charge funnelling

194 The main losses in a photovoltaic device are given by two factors: (1) lack of absorption of
195 photons with energy E smaller than the bandgap of the photoactive material E_g and (2)
196 dissipation of the kinetic energy of carriers with energy $E \gg E_g$. The first process accounts
197 for 23 % of the energy of the sun whilst the second for 33 %.[15] Charge funnelling can tackle
198 both problems. A solution to the first problem has been proposed based on multiple-bandgap
199 tandem solar-cells. With this respect, funnelling offers the ability to continuously tune the
200 bandgap of the active material, effectively realizing a continuous tandem solar cell. The
201 second factor is related to carrier dynamics: after photon absorption carriers are excited in
202 a distribution which mimics the energy distribution of the photons. After a few hundred
203 femtoseconds, carrier-carrier scattering equilibrates this distribution to a population which
204 can be described by a temperature T_H. In the following tens of picoseconds, carriers loose
205 kinetic energy via phonon emission and relax to a distribution in quasi-equilibrium with
206 the lattice temperature T_a, a process known as cooling. After this, carriers recombine in
207 different ways to return the system to equilibrium. This dynamics is taken into account in
208 estimating the Shockley-Queisser[16]limit by considering that carriers are completely cooled
209 when extracted at temperature T_a, for a given bandgap. This calculation gives a theoretical
210 limit of $\sim 31\,\%$ efficiency for a bandgap of $E_g \sim 1.3\,\mathrm{eV}$, under the illumination of a blackbody
211 equivalent to 1 Sun at 5760 K.

212 As we show in our work, inverse charge funnelling reduces the recombination lifetime
213 of photoexcited carriers from $10^{-10}\,\mathrm{s}$ to $10^{-6}\,\mathrm{s}$. Furthermore, thanks to the modulation
214 of the bandgap and the consequent built-in field in the strain region, the drift velocity is
215 expected to increase. The cooling rate of electrons and holes is inversely proportional to
216 the relaxation time whilst the recombination lifetime is proportional to it.[17] Therefore, the
217 observed reduction of the recombination lifetime can be related to the slowing of the cooling

218 process, which, together with the increased drift velocity, allow the distribution of hot carriers
219 to be maintained at a temperature T_h, where $T_H > T_h > T_a$. The exploitation of hot-carriers
220 extraction has been largely investigated and the maximum efficiency of a photovoltaic device
221 can be theoretically estimated[15] to be $\sim 65\,\%$ at $E_g \sim 0.5\,\mathrm{eV}$, under the illumination of a
222 blackbody equivalent to 1 Sun at 5760 K, for a carrier temperature of 3600 K. It is possible
223 to compute such limit for the case of HfS_2. The estimation of the maximum efficiency
224 of a hot-carrier solar cells relies on a number of assumptions, which should carefully be
225 reviewed in light of what is achievable in a funnel device. One of the main assumptions
226 is that the extraction of carrier is performed with selective contacts which have an energy
227 separation between holes and electrons larger than the bandgap ($E_{out} > E_g$, ideally close to
228 the median energy of the hot-electrons distribution) and that extraction is performed in an
229 extremely narrow energy range ($\Delta E_{out} \ll k_B T$). The realization of such effect has been the
230 subject of many studies and attempts to realise hot-carrier extraction using, for example,
231 quantum-confined structures have been reported.[18,19] By taking the above discussion into
232 consideration, it is possible to calculate the current extracted from a hot carrier solar cell:

$$J \cdot E_{out} = q\left[f_s L(E_g, \inf, T_a, 0) - L(E_g, \inf, T_h, \mu_h) + (1 - f_s) L(E_g, \inf, T_a, 0)\right], \tag{S13}$$

233 where J is the current density, $f_s = 2.16 \cdot 10^{-5}$ is the angular range of the sun, q is the charge
234 of the electron, μ_h is the chemical potential of the hot electrons and $L(E_min, E_max, T, \mu)$ rep-
235 resents the net emitted or absorbed energy flux density integrated over the range $[E_{min}, E_{max}]$
236 and it is equal to

$$L(E_{min}, E_{max}, T, \mu) = \frac{2\pi}{h^3 c^2} \int_{E_{min}}^{E_{max}} \frac{E^3}{e^{\frac{E-\mu}{k_B T}} - 1} dE, \tag{S14}$$

237 where h is the Planks constant, c the speed of light and k_B the Boltzmanns constant. The
238 first term in equation (S13) represents the energy flux density received by the sun, the

239 second term represents the energy flux density absorbed by the solar cell and the third term
240 represents the energy flux density emitted by the solar cell into the environment (detailed
241 balance limit). From the $J(V)$ curve it is possible to calculate the extracted power $P(V) =$
242 $V \cdot J$ from the solar cell and, consequently, the maximum efficiency given the three design
243 parameters E_g,E_{out} and V. Our calculation shows that, for a carrier temperature of 2000 K
244 it is possible to achieve a maximum efficiency of $\sim 45\,\%$ for a bandgap of 1.96 eV (HfS_2),
245 assuming extraction at the contacts with energy ~ 0.2 eV above the bandgap. Such electron
246 temperature has indeed be reported in graphene[20] and the required type of contacts could
247 be realised, for example, using heterostructures of 2D materials in order to achieve the
248 desired band-alignment.[21] A smaller bandgap can give a higher efficiency, up to 65 %. Such
249 requirement can be easily satisfied in a funnel device owing to the ability of TMDs to
250 sustain levels of strain up to 11 %[22] and the strong layer-dependent bandgap, which has
251 been demonstrated in many 2D materials.[23,24]

252 ## References

253 (1) Memming, R. *Semiconductor Electrochemistry*; Wiley, 2008.

254 (2) Favron, A.; Gaufres, E.; Fossard, F.; Phaneuf-L'Heureux, A.-L.; Tang, N. Y.-W.;
255 Levesque, P. L.; Loiseau, A.; Leonelli, R.; Francoeur, S.; Martel, R. Photooxidation
256 and quantum confinement effects in exfoliated black phosphorus. *Nat Mater* **2015**, *14*,
257 826–832.

258 (3) Iwasaki, T.; Kuroda, N.; Nishina, Y. Anisotropy of Lattice Dynamical Properties in
259 ZrS_2 and HfS_2. *Journal of the Physical Society of Japan* **1982**, *51*, 2233–2240.

260 (4) Cingolani, A.; Lugar, M.; Scamarcio, G.; Lvy, F. The Raman scattering in hafnium
261 disulfide. *Solid State Communications* **1987**, *62*, 121 – 123.

262 (5) Roubi, L.; Carlone, C. Resonance Raman spectrum of HfS_2 and ZrS_2. *Phys. Rev. B*
263 **1988**, *37*, 6808–6812.

264 (6) Greenaway, D.; Nitsche, R. Preparation and optical properties of group IV-VI chalco-
265 genides having the CdI_2 structure. *Journal of Physics and Chemistry of Solids* **1965**,
266 *26*, 1445 – 1458.

267 (7) Nath, M.; Rao, C. N. R. Nanotubes of Group 4 Metal Disulfides. *Angewandte Chemie*
268 *International Edition* **2002**, *41*, 3451–3454.

269 (8) Traving, M.; Seydel, T.; Kipp, L.; Skibowski, M.; Starrost, F.; Krasovskii, E. E.;
270 Perlov, A.; Schattke, W. Combined photoemission and inverse photoemission study
271 of HfS_2. *Phys. Rev. B* **2001**, *63*, 035107.

272 (9) Rasmussen, F. A.; Thygesen, K. S. Computational 2D Materials Database: Electronic
273 Structure of Transition-Metal Dichalcogenides and Oxides. *The Journal of Physical*
274 *Chemistry C* **2015**, *119*, 13169–13183.

275 (10) Chae, S. H.; Jin, Y.; Kim, T. S.; Chung, D. S.; Na, H.; Nam, H.; Kim, H.; Perello, D. J.;
276 Jeong, H. Y.; Ly, T. H.; Lee, Y. H. Oxidation Effect in Octahedral Hafnium Disulfide
277 Thin Film. *ACS Nano* **2016**, *10*, 1309–1316.

278 (11) Graham, R.; Yu, D. Scanning Photocurrent Microscopy in Semiconductor Nanostruc-
279 tures. *Modern Physics Letters B* **2013**, *27*, 1330018.

280 (12) Feng, J.; Qian, X.; Huang, C.-W.; Li, J. Strain-engineered artificial atom as a broad-
281 spectrum solar energy funnel. *Nat Photon* **2012**, *6*, 866–872.

282 (13) Xu, K.; Wang, Z.; Wang, F.; Huang, Y.; Wang, F.; Yin, L.; Jiang, C.; He, J. Ultra-
283 sensitive Phototransistors Based on Few-Layered HfS_2. *Advanced Materials* **2015**, *27*,
284 7881–7887.

285 (14) San-Jose, P.; Parente, V.; Guinea, F.; Roldán, R.; Prada, E. Inverse funnel effect of
286 excitons in strained black phosphorus. *Physical Review X* **2016**, *6*, 1–12.

287 (15) Nelson, J. *The Physics of Solar Cells*, 1st ed.; Imperial College Press, 2011; Chapter
288 10, pp 289–325.

289 (16) Shockley, W.; Queisser, H. J. Detailed Balance Limit of Efficiency of p-n Junction Solar
290 Cells. *Journal of Applied Physics* **1961**, *32*, 510–519.

291 (17) Sánchez, M. Carrier heating or cooling in semiconductor devices. *Solid-State Electronics*
292 **1973**, *16*, 549 – 557.

293 (18) Nozik, A. J. Spectroscopy and hot electron relaxation dynamics in semiconductor quan-
294 tum wells and quantum dots. *Annual Review of Physical Chemistry* **2001**, *52*, 193–231.

295 (19) Watanabe, D.; Kasamatsu, N.; Harada, Y.; Kita, T. Hot-carrier solar cells using low-
296 dimensional quantum structures. *Applied Physics Letters* **2014**, *105*, 171904.

297 (20) Johannsen, J. C.; Ulstrup, S.; Cilento, F.; Crepaldi, A.; Zacchigna, M.; Cacho, C.;
298 Turcu, I. C. E.; Springate, E.; Fromm, F.; Raidel, C.; Seyller, T.; Parmigiani, F.;

299 Grioni, M.; Hofmann, P. Direct View of Hot Carrier Dynamics in Graphene. *Phys.*
300 *Rev. Lett.* **2013**, *111*, 027403.

301 (21) Özçelik, V. O.; Azadani, J. G.; Yang, C.; Koester, S. J.; Low, T. Band alignment of
302 two-dimensional semiconductors for designing heterostructures with momentum space
303 matching. *Phys. Rev. B* **2016**, *94*, 035125.

304 (22) Bertolazzi, S.; Brivio, J.; Kis, A. Stretching and Breaking of Ultrathin MoS2. *ACS*
305 *Nano* **2011**, *5*, 9703–9709.

306 (23) Xia, F.; Wang, H.; Jia, Y. Rediscovering black phosphorus as an anisotropic layered
307 material for optoelectronics and electronics. *Nature Communications* **2014**, *5*, 4458.

308 (24) Wang, Q. H.; Kalantar-Zadeh, K.; Kis, A.; Coleman, J. N.; Strano, M. S. Electron-
309 ics and optoelectronics of two-dimensional transition metal dichalcogenides. *Nat Nano*
310 **2012**, *7*, 699–712.